한국가시화정보학회지, 제3권, 제1호, (2005) 3~19
<특집기사 논문>

# Optical Tracking of Three-Dimensional Brownian Motion of Nanoparticles

C. K. Choi and K. D. Kihm†

**Abstract.** Novel optical techniques are presented for three-dimensional tracking of nanoparticles; Optical Serial Sectioning Microscopy (OSSM) and Ratiometric Total Internal Reflection Fluorescent Microscopy (R-TIRFM). OSSM measures optically diffracted particle images, the so-called Point Spread Function (PSF), and determines the defocusing or line-of-sight location of the imaged particle measured from the focal plane. The line-of-sight Brownian motion detection using the OSSM technique is proposed in lieu of the more cumbersome two-dimensional Brownian motion tracking on the imaging plane as a potentially more effective tool to nonintrusively map the temperature fields for nanoparticle suspension fluids. On the other hand, R-TIRFM is presented to experimentally examine the classic theory on the near-wall hindered Brownian diffusive motion. An evanescent wave field from the total internal reflection of a 488-nm bandwidth of an argon-ion laser is used to provide a thin illumination field of an order of a few hundred nanometers from the wall. The experimental results show good agreement with the lateral hindrance theory, but show discrepancies from the normal hindrance theory. It is conjectured that the discrepancies can be attributed to the additional hindering effects, including electrostatic and electro-osmotic interactions between the negatively charged tracer particles and the glass surface.

**Key Words:** Optical Serial Sectioning Microscopy (OSSM), Ratiometric Total Internal Reflection Fluorescent Microscopy (R-TIRFM), Brownian Motion, Diffusion

## 1. Introduction

Single molecule detection (SMD) techniques to visualize the dynamic behavior and reaction kinetics of individual molecules in living cells have recently attracted a great deal of attention[1, 2]. The rapid development and progress of SMD techniques have ushered in a revolution in biological research. Stochastic characteristics of reactions of biological molecules, even if the reactions of biomolecules are initiated at the same time, cannot be synchronized as a result of which dynamic behaviors of individual molecules are averaged and hidden in the ensemble-averaged movements[3]. SMD is generally based on two key technologies, single molecule imaging and single molecule manipulation. But there are certain optical issues associated with the detection and subsequent tracking of single molecules. The size of individual molecules is on the order of nano-meters and so they are too small to be visualized by conventional optical microscopy. To overcome this problem, bio-molecules are labeled by fluorescence dyes and visualized using fluorescence microscopy.

The non-invasive nature of the fluorophores associated with the high sensitivity and contrast has made fluorescence microscopy a prominent tool in modern cell biology[4]. However, a significant drawback of light microscopy is dictated by the laws of diffraction. The limit of resolution that can be reached by optical techniques is directly proportional to the wavelength of incident light[5]. This diffraction limit originates from the fact that it is impossible to focus a beam of light to a spot smaller than approximately its wavelength. Therefrom here are two possible research areas as fol-

†Magnavox Professor and Director of Micro/Nano-Scale Fluidics and Energy Transport Laboratory
E-mail: kkihm@utk.edu
Department of Mechanical, Aerospace, and Biomedical Engineering University of Tennessee, Knosville, TN 37996, USA

lowing; one is to utilize this optical drawback of diffraction, and the other is to break this diffraction limit with the development of several novel imaging techniques.

The OSSM technique utilizes a standard epi-fluorescence microscopy with a high numerical aperture objective to record and analyze the 3-D diffraction image patterns of small particles[6], originally developed to obtain a 3-D depthwise resolved image in a thick biological specimen[7]. The wave nature of light images a point source to form a diffraction pattern that is longitudinally modulating with respect to the focal plane and laterally modulating with respect to the optical axis. The resulting 3-D image pattern is expressed in a fully analytical form of a symmetric vector function in the absence of optical aberration[8-9]. However, optical aberrations caused by any non-ideal specimen structures bring about complicated asymmetric image patterns[10]. An experimental verification of the analysis has been conducted by using an advanced video microscopy system and the Gibson and Lanni's equation is applied for a dry objective system, and 3-D intensity profiles of fluorescent microspheres were measured by using a computational optical sectioning microscopy[11,12]. A similar idea for tracking 3-D particles using off-focus imaging[13] was presented, where an experimental correlation between the diffraction pattern and the defocusing distance was used.

Total Internal Reflection Fluorescence Microscopy (TIRFM) uses an electromagnetic field called the 'evanescent field', in the rarer medium from the denser medium at a high incident angle[5,14], to excite the fluorophores within several hundred nanometers from the interface[15,16]. This leakage of electro-magnetic field, popularly called the evanescent wave or field, undergoes exponential intensity decay with increasing distance from the surface[6]. This method provides a significant improvement for near field illumination compared to differential interference contrast[11], confocal microscopy[17], theta microscopy[18] or multi-photon microscopy [19]. TIRFM has been a popular technique for both *in vitro* and *in vivo* single molecule detection[3, 20], based on a narrow and optically defined excitation depth most effectively to overcome the background noise problem[21].

Very recently, the first microfluidic application of prism-based TIRFM is proposed to measure the near-wall flow fields for a rotating Couette flow [22]. Shortly after that, the use of a special TIRF objective lens was presented to measure the Brownian motion under various flow shear conditions[23]. This study is a nice example to use TIRFM for study of near-wall particle diffusive motion, however, the measurement scope is limited to two-dimensional in nature, similar to the former study. The out of plane examination of the Brownian motion will be needed to further investigate the near-wall hindered diffusion that is inherently three-dimensional.

The current paper presents OSSM[6,7] and ratiometric TIRFM principles[24,25], respectively; (I) OSSM is nonintrusive thermometry and 3-D tracking using optical diffraction pattern in all domain a little away from the surface, and (II) R-TIRFM experimentally validates and examines the near-wall hindered diffusion theory fully in three-dimensional mode, in the extremely near region to a solid surface. A robust Neural Network model to track particle pairs has been also developed to simultaneously measure three-dimensional Brownian diffusive motions of nanoparticles. The experimental findings clearly evidence the theory of near-wall hindered diffusion particularly within sub-micron ranges from the solid wall surface. The measurement results are compared with the Stokes flow model for diffusion[26] and the hindered diffusion theories[27-29].

## 2. Brownian Motion of Nanoparticles

In micro-PIV (Particle Image Velocimetry)/PTV (Particle Tracking Velocimetry) applications at low Reynolds numbers, the magnitude of the Brownian thermally diffusive motion can be comparable to the convective flow displacement itself[30]. It has been shown that the well-defined thermal correlation of the Brownian motion can be used for nonintrusive temperature measurement schemes[31-33]. Based on the fact that the kinetic potential energy of molecules, or extremely fine particles, shows an inverse-linear dependence on temperature, namely 1/2kT, a correlation between Brownian motion and temperature was established.

The observation of random motion was first reported by Jan Ingenhousz[34] and was subsequently rediscovered and named after the eminent botanist Robert Brown who noted the random motion of pollen particles under a microscope[35]. Albert Einstein used the kinetic theory to derive the diffusion coefficient for such motion in terms of fundamental parameters of the particles and liquid for his well-known doctoral dissertation, "Annus Mirabilis," published in 1905. Perrin, in 1908, attempted to verify the theory by painstakingly measuring the time dependence of one and two-dimensional mean square displacements of microscale grains of a known size in a fluid[36,37]. More recently, the use of video microscopy has allowed two-dimensional tracking of Brownian motion of suspended particles with substantially shorter time intervals than in Perrin's experiment. Calculation of the mean square displacements of the data has shown good correlation with Einstein's theoretical values[38,39]. It is well known that Einstein's theory predicts the Brownian motion with acceptable accuracy for one- and two-dimensions by evaluating the mean square displacement in terms of the Avogadro's number. The classical theory of Einstein applies to suspensions, which are effectively so dilute that each particle is moving alone in an infinite fluid. The particle can be assumed to be a sphere that is large compared to the molecules of the fluid (solvent). Thus, the frictional resistance of the particle can be calculated taking into consideration ordinary particle hydrodynamics. Within the limits of ordinary hydrodynamics, the net resistance force or viscous drag force, $F_d$, on the particle is given by Stokes Law as

$$F_d = 3\pi\mu d_p u_d \tag{1}$$

The three-dimensional MSD of the random walk traveled by suspended particles is expressed as:

$$\langle \Delta r^2 \rangle = \frac{\sum_{i=1} \Delta r_i^2}{n} = \frac{\sum_{i=1} (\Delta x_i^2 + \Delta y_i^2 + \Delta z_i^2)}{n} = 6D\Delta t \tag{2}$$

where $D$ indicates the Brownian thermal diffusivity (or equivalently a diffusion coefficient) of the particle suspended in the fluid and $\Delta t$ is an observation time interval of each incremental displacement. The observation time interval may be equated to the image frame interval of a CCD camera as long as the frame rate is sufficiently high to discern the minutely changing displacements of the random walk. Note that the mean displacement $\langle \Delta r \rangle$ of the particle vanishes because of the spherical symmetry of random motion and contains no information on $D$ [40]. Thus, the diffusion coefficient $D$ for a dilute suspension of particles as originally defined by Einstein in 1905 is written as

$$D = \frac{kT}{3\pi\mu d_p} \tag{3}$$

where $k$ is Boltzman's constant ($1.3805 \times 10^{-23}$ J/K), $T$ is the absolute temperature, and $\mu$ is the dynamic viscosity of the fluid and is expressed as [41];

$$\mu = 2.414 \times 10^{-5} \times 10^{\frac{247.8}{T-140}} \text{ (for water)} \tag{4}$$

The Brownian diffusivity, and the corresponding MSD of a particle with a known size, can be uniquely determined by the suspension temperature. Conversely, by measuring the Brownian diffusivity of the suspended particle, the surrounding liquid temperature can be readily determined with the equation of diffusion coefficient depending on temperature only for fixed particle diameter. Recently, using a simple video microscopy[38,39], the elementary one- and two-dimensional Brownian motions have been examined for freely diffusing 1.02-μm polystyrene spheres suspended in water to show the validity of the Einstein relationship and inversely determine the Boltzman's constant. However, it should be kept in mind that a diffusion equation does not provide information on the particle trajectory[41].

The particle hydrodynamics changes significantly if the particle is present close to a solid wall. It has been found that the dynamics of the particles close to the wall become significantly non-Gaussian and the average particle displacement differs from the theoretical most probable particle displacement. The presence of these boundaries at finite distances from the particle necessitates the corrections to the Stokes' resistance formula. Brenner provided an analytical expression in the form of an infinite series for this correction term[28]. He used a hypoth-

esis of no relative motion at the fluid solid interface. By using an analogy of evanescence of velocity at the plane wall, Brenner refined his boundary conditions and solved the resulting Navier Stokes Equation for a creeping flow to derive the correction parameter $x$ for the correction of the diffusion coefficient in the normal direction. Thus, the "hindered" one-dimensional normal diffusion coefficient $D_\perp$ of a spherical particle at a base distance $h$ from the wall can be written as:

$$D_\perp = \xi \frac{kT}{3\pi\mu d_p} = \xi \cdot D \tag{5}$$

The findings of Brenner has been supported by a number of authors who have highlighted the need for a correction to the Stokes law for a particle close to a wall or for the case where there are two or more particles close to each other[43].

Goldman *et al.*[27] analyzed the slow viscous motion of the sphere parallel to a plane wall bounding a semi-infinite, quiescent, and viscous fluid and used an asymptotic solution of the Stokes Equation for rotational and translational motion close to the wall. Using an analogy corresponding to a translational lubrication-theory, corrected values of tangential forces and torques on the spherical particle have been evaluated. Considering the resulting correction parameter ($\beta$) for the tangential force as a result of the presence of the solid wall, the "hindered" tangential diffusion coefficient $D_{||}$ of a spherical particle at a distance $h$ from the wall can be written as:

$$D_{||} = \beta \frac{kT}{3\pi\mu d_p} = \beta D \tag{6}$$

However, since the particle tracking is performed in three dimensions, it becomes important to define a bulk hindered diffusion coefficient. Keeping in mind that the Einstein-Smoluchowski Equation gives: $\langle x^2\rangle=\langle y^2\rangle=\langle z^2\rangle=2Dt$, we get the correction factor for the bulk three-dimensional diffusion coefficient as:

$$D_o = \psi D \ with \ \psi = \frac{2\beta+\xi}{3} \tag{7}$$

where the arithmetic addition of all three directional components of MSD constructs the total or bulk MSD as shown in Eq. (2). The values of $\xi$, $\beta$, and $\psi$ for a particle diameter of 200nm and for various elevations from the base of the sphere are shown in Fig. 1. Note that inter particle interaction is kept to a minimum in the experiment by taking a volume fraction of 0.001%, based on Batchelor [44]. It should also be noted that, the experimentally determined MSD represents an average for a number of particles at different $z$-locations, while the correction coefficients $\xi$, $\beta$ and $\psi$ are proposed for a single particle at a specified depth $h$. Therefore, averaged values of the correction coefficients (Fig. 1) for the whole penetration depth have been used to correct the experimental data obtained for the near-wall regions.

For the case of the near wall region (less that 1 μm from the wall), a Ratiometric Total Internal Reflection Fluorescence Microscopy (R-TIRFM) has allowed simultaneous three-dimensional tracking of nanoparticles for their near-wall "hindered" Brownian motion[45], while Optical Serial Sectioning Microscopy (OSSM) detects three-dimensional "unhindered" or free Brownian motion outside the near-wall region. The OSSM method uses the optical diffraction patterns of focused and defocused images of nanoparticles and compares them to the theoretically predicted patterns so that the location of the particle can be identified with respect to the focal plane of the imaging optics.

## 3. Optical Serial Sectioning Microscopy (OSSM)

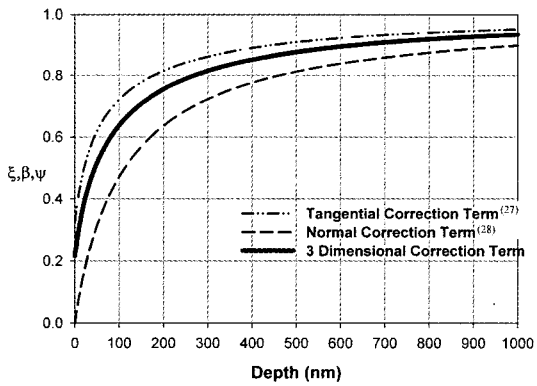


**Fig. 1.** Correction Factors for Bulk, Normal, and Tangential Diffusion Coefficient as the particle approaches the wall ($d_p$ = 200 nm)[46].

OSSM technique is not only to demonstrate three-dimensional tracking of Brownian motion of submicron tracer particles by analyzing the optical diffraction images but also to implement a concept for an *in-situ* and full-field mapping thermometry with microscale resolution based on the temperature correlation with the measured Brownian diffusivity of nanoparticles, based on Einstein's theory for the range of temperature from 5 to 70°C.

### 3.1 Point Spread Function (PSF) and Optical Serial Sectioning Microscopy (OSSM)

When a point source or small particle is imaged through an aperture or high-magnification objective lens, the phase modulation based on the wave nature of light forms a spatially distributing diffraction pattern. The three-dimensional diffraction pattern is called a Point Spread Function (PSF) and is generated from stacks of serial optical sections[6]. Another important factor to consider is optical aberrations, which occur when the imaging is conducted under "off-design" conditions. In practice significant aberration is commonly caused by two variables: one, the different refraction indices of the cover glasses and immersion media, and two, the variability in the thickness of the immersion media and cover glass from the specified design values. A monochromatic spherical wave emitting from a point source transverses the entrance pupil of an objective lens and emerges from the exit pupil of the objective lens, and converges towards the back focal point (Fig. 2-a). The analytical form of PSF based on the *Huygens-Fresnel Interference Principle* consists of the Bessel function and a sinusoidal complex exponential term, both of which essentially constitute the modulation of PSF in the lateral and in the line-of-sight directions, respectively. Figure 2-a illustrates an aberration-free imaging system with the design conditions (*). Note that the specimen thickness ($t_{s*}$) should be zero to ensure the aberration-free imaging. When these conditions are not met, the refracted rays have optical pathways that deviate from the original aberration-free conditions and do not converge to the ideal focal point. In consequence, the refraction due to the index mismatching affects the optical aberration of an objective lens and produces asymmetric diffraction patterns as schematically illustrated in Fig. 2-b. Since the aqueous medium of a specimen, in general, has a different refractive index from those of a cover glass and of an immersion medium, most practical cases are subject to asymmetric PSF images.

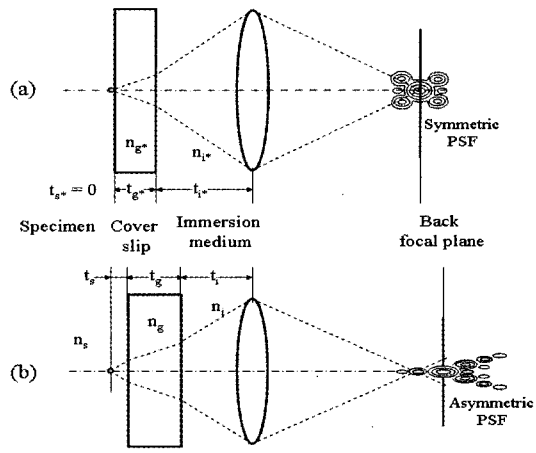


**Fig. 2.** Formation of Point Spread Function (PSF): (a) aberration-free imaging to form a symmetric PSF; and (b) aberrated imaging to form an asymmetric PSF[57].

Gibson and Lanni presented a comprehensive form of PSF on a basis of Kirchhoff's diffraction integral formula[10]. The three-dimensional intensity distribution of PSF is expressed in terms of the detector location ($x_d$, $y_d$), the numerical aperture of the objective lens ($NA$), the magnification of the microscopy system ($M$), and the defocus distance ($\Delta z$) as:

$$I(x_d, d_d, \Delta z) = \left| C \int_0^1 J_0\left[ k \frac{NA}{\sqrt{M^2 - NA^2}} \rho \sqrt{x_d^2 + y_d^2} \right] \exp[jW(\Delta z, \rho)] \rho \, d\rho \right|^2 \quad (8)$$

where $k$ is the wave number ($2\pi/\lambda$) with $\lambda$ being the emission wavelength of a point source, is the normalized radius in the exit pupil, and $W(\Delta z, r)$ is a phase aberration function, which is the product of the Wave Number ($k$) and optical path length difference (OPD). The three-dimensional PSF of Eq. (8) is reduced to the planar Airy function[5] on the focal plane at $\Delta z = 0$ and the resulting intensity pattern modulates in the radial and axi-symmetric directions. The PSF of Eq. (8) also modulates in

the line-of-sight axial direction as it can be demonstrated for the case of $x_d = 0$ and $y_d = 0$.

The principle of OSSM is based on the determination of the radial intensity profile normal to the meridional plane as a function of $\Delta z$. In other words, the relative line-of-sight ($z$) location of a particle measured from the focal plane can be determined by observing the radial diffraction pattern, in particular the increase in the out-most fringe radius with an increase in defocusing distance. The out-most fringes are identified with less uncertainty in general for the asymmetric case, because of their brighter and narrower definition.

### 3.2 Experiment

The most crucial part of the experiment is to ensure the calibration accuracy of the OSSM-measured radial intensity profiles in comparison with the calculated intensity profiles based on Eq. (8). The OSSM calibration system (Fig. 3) consists of an epi-fluorescent microscope (upright Olympus BX 61 Model) with a dry objective lens (40X, 0.75 N.A.), a 1024 × 1024 pixel CCD camera (UNIQ Vision Inc., UP-1830) with a frame grabber at 30 fps (QED-Imaging Inc.), and a 170 μm high calibration chamber. Yellow-green (505/515) fluorescent polystyrene micro-spheres, with a nominal diameter of 500 ± 16 nm and a density of 1.05-g/ml (Molecular Probes Inc.), are used as tracers. The calibration chamber is filled with a water-based solution at a volume concentration of $4 \times 10^{-6}$ of the seeding particles and the calibration experiment is conducted at the laboratory temperature of 22°C. Extra care is taken to minimize particle coagulations by dispersing the sample extensively using a sonicator before and after conducting each experiment.

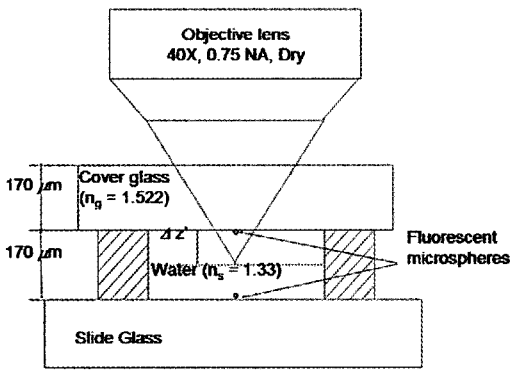


**Fig. 3.** Schematic of a test specimen for measuring both symmetric and asymmetric PSFs in the OSSM using 500±16 nm nominal diameter Nanoparticles[57].

When a test particle is located at the top glass plate, the chamber is to provide a nearly aberration-free condition. This in turn will form a symmetric PSF in the absence of the specimen thickness ($t_{s^*}$), which is the primary source of aberration for most cases. On the other hand, when a test particle is located at the bottom plate, the thickness (170 μm) of the specimen creates a substantial aberration effect to make asymmetric diffraction patterns necessary for the particle. Note that $\Delta z'$ in Fig. 3 is the location of the actual imaging plane that is compensated for by the refractive index mismatching occurring throughout the imaging rays whereas $\Delta z$ in Eq. (8) is the mechanical movement of the objective controlled by a stage with 1 μm resolution. Thus, the defocusing distance ($\Delta z'$) is varied with 1.33 μm resolution. For the case of the top particle, the calibration is conducted to establish a correlation of the symmetric PSFs with a negative defocusing distance for particles located at a shorter distance than the focal distance as the objective is lowered from the initial focusing point of the top surface. For the case of the bottom particle, a calibration for the asymmetric PSF is conducted for a positive defocusing distance for particles located beyond the focal plane as the objective is lifted from the bottom focal plane.

The second test chamber is designed to measure the thermal effect on the particle's Brownian motion. The chamber is geometrically similar to the calibration chamber. One change however is that a steady temperature condition is provided for the test fluid by embedding the test chamber in a copper block with a coolant passage built in. This enables the coolant to be circulated to and from a constant thermal bath. A thermo-couple probe is flush-installed at the inside bottom surface to monitor the liquid temperature. Another important modification is that the test chamber uses an off-designed cover glass of 223 μm thickness in order to construct asymmetric PSFs in a more pronounced way. The focal plane of the objective lens is fixed to the top glass-water interface and any

suspended particles can generate asymmetric PSF images for all experiments. This is possible because of the off-designed cover glass and the suspension medium (water) of mismatching refractive index. It is more realistic to assume that a nonzero specimen distance ($t_s$) is the condition in most practical imaging cases as particles are suspended and imaged in a liquid medium.

### 3.3 Measured and calculated PSF profiles versus defocus distance (Δz')

The top inset plot in Fig. 4 shows the correlation between the out-most fringe diameter ($D_{OMF}$) of the PSF diffraction images constructed by a single 500-nm particle with the line-of-sight location measured from the focal plane, or equivalently the defocusing distance (Δz'). The focal plane at Δz' = 0 is defined as the upper (or closer to the objective) inner wall of the cover glass for the symmetric case, and as the lower inner wall for the asymmetric case. The defocusing distance is varied by altering the vertical location of the microscopic objective with respect to the zero point corresponding to the focal plane. The symbols represent the measured diameters of the out-most rings of the fringe patterns and the dashed curves correspond to the calculated diameters of the last peaks of PSFs based on Eq. (8).

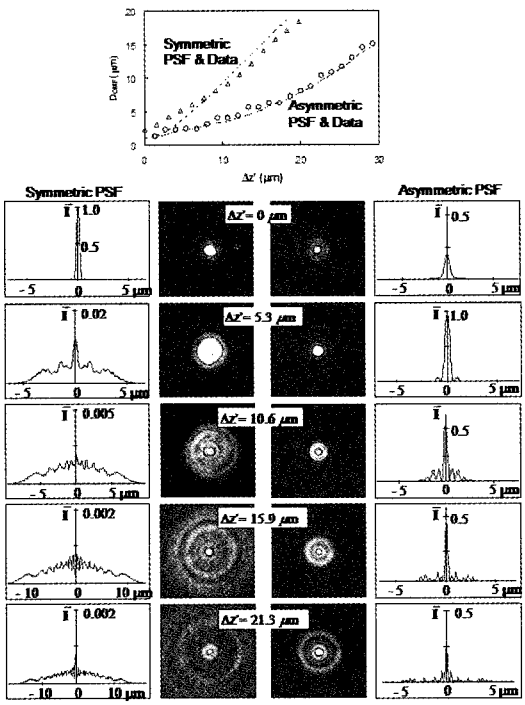


**Fig. 4.** The symmetric and asymmetric 3-D diffraction patterns of a 500-nm diameter particle imaged by OSSM and the corresponding predictions for normalized radial intensity distribution based on the theoretical model of Gibson and Lanni[57].

The measured diffraction images of the inset photos are observed to determine the diameters of out-most bright rings at 1.33 μm intervals of Δz'. Also, a series of calculated intensity distributions, as shown next to each corresponding photo, are obtained at the same interval of Δz' and the last peaks of the intensities representing the out-most fringe locations are searched. The design conditions for the symmetric case are $t_s^*$ =0 mm, $t_g^*$ = 0.17 mm, $t_i^*$ = 0.51 mm, $n_g^*$ = 1.522, and $n_i^*$= 1.0. The off-design conditions for the asymmetric case are $t_s$ = 0.17 mm, $t_g$ = 0.17 mm, $t_i \approx$ 0.38 mm, $n_g$ = 1.522, and $n_i$ = 1.0. For both the symmetric and asymmetric cases, the measured out-most diameters show fairly good agreement with the calculated values at the same defocusing distance of Δz'. Therefore, the line-of-sight displacement Δz' of suspended particles can now be determined by optimally fitting the measured out-most fringe diameter to the calculated PSF profiles.

### 3.4 Simultaneous measurements of three-dimensional Brownian motion

Figure 5-a shows instantaneous diffraction patterns of monodisperse 500-nm (±16 nm) diameter polystyrene fluorescent particles suspended in water. Different out-most fringe diameters indicate their three-dimensional distribution with different $z$-locations. The objective lens is focused on the top inner glass surface and the particles are suspended in water below the focal plane with the $z$-coordinate in the downward direction (refer to Fig. 3). Fig. 5-a indicates the depthwise $z$-locations of the individual particles measured by fitting the out-most ring diameter data to the corresponding calibration curve given by Eq. (8). The $x$-$y$ locations are determined by manually tracking the planar movement of the geometrical centers of fringes on the two-dimensional image plane. Figure 5-b shows

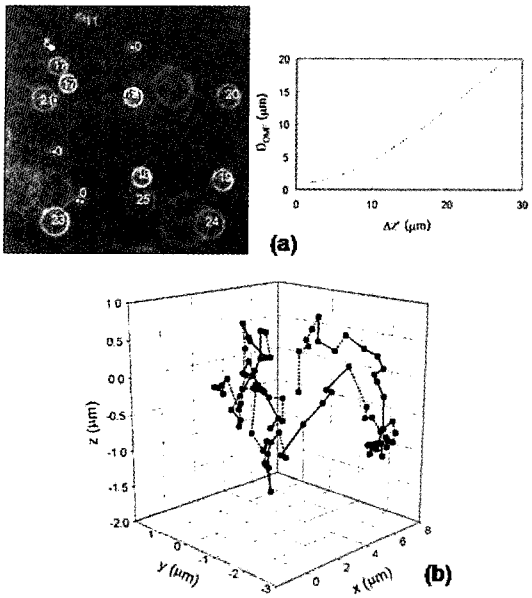


**Fig. 5.** (a) Measured diffraction patterns of 500-nm diameter polystyrene fluorescent particles suspended in water at 25°C with numeric values indicating the depthwise z-locations in μm, and (b) measured three-dimensional Brownian motion of a single particle at 33ms time intervals (solid lines indicate upward movement and dashed lines indicate downward movement)[57].

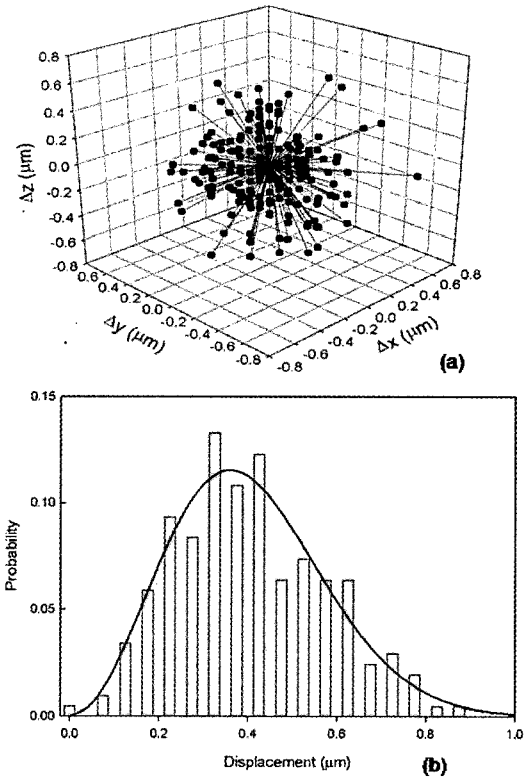


**Fig. 6.** (a) The distribution of three-dimensional displacements for all 203 steps of 7 particles at 25 °C. (b) The step time interval is 33-ms and the bin width is 0.05 μm. The three-dimensional probability curve fit is based on the form listed in Eq. (12)[57].

the measured trajectory of an arbitrarily selected single particle under thermal Brownian motion in water at 25°C for the measurement period of three seconds at 30 fps. Solid line segments indicate upward particle movement and the dashed line segments indicate downward movement. Analyzing the particle images using OSSM principle permits the fully three-dimensional tracking of nanoparticles in submicron resolution. The spatial resolution for displacement measurements should be limited by the discrete nature of pixel array data of the imaging CCD array. The *x*-*y* measurement resolution is estimated to 0.16 μm based on the imaging magnification (40X) and the physical pixel resolution (6.45 μm) of the CCD chip. The line-of-sight *z* resolution can be estimated by accounting for the sensitivity of the out-most ring diameter to the defocus distance. One pixel deviation in determining the out-most diameter renders approximately 0.16 μm in Δz', and thus, the *z* measurement resolution is also estimated to about 0.16 μm.

Figure 6-a shows the directions and magnitudes of the three-dimensional displacements shown in Fig. 5-b. As anticipated, the spherical distribution of their directions and magnitudes reflects the anisotropic random nature of unhindered Brownian motion. In Fig. 6-b, the corresponding probability histogram of the measured displacements is shown with the predicted Gaussian or random probability distribution as:

$$p(\Delta r,\Delta t)=\frac{4\pi\Delta r^2}{8(\pi D\Delta t)^{3/2}}e^{-\Delta r^2/4D\Delta t} \tag{9}$$

where the 3-D Displacement is $\Delta r=\sqrt{(\Delta x^2+\Delta y^2+\Delta z^2)}$. $\Delta x$, $\Delta y$, and $\Delta z$ are elementary one-dimensional displacements, respectively, $D$ is the Brownian diffusivity given by Eq. (3), and $\Delta t$ is the time interval between displacement measurements

(33 ms). The resulting 3-D probability curve fit shows the statistical validation of the present Brownian motion detection for over two hundred realizations.

### 3.5 Consideration of critical microscale factors

Care has been taken to account for the bias factors that can possibly alter the temperature dependence of the Brownian motion, i.e. thermal convection effects, particle sedimentation, and particle-to-particle interactions. The Rayleigh number ($\equiv g\beta\Delta TL^3/an$) was calculated to be 22.1 much less than the critical value of 1708[47]. Therefore it can be assumed that buoyant forces do not affect the fluid inside the chamber. The calculated Peclet number ($Pe = 2aU_0/D_0 = 8\pi a^4\Delta\rho g/3k_BT$) varies from 0.00418 to 0.0034 for the tested temperature range from 5 to 70°C. So, it is expected that the Brownian motion is free from the sedimentation bias effect. From the volume concentration of presently seeded nanoparticles of $4\times10^{-6}$, the average interparticular distance is calculated to be approximately 25.8 which is more than one hundred (100) times of the seeding particle radius of 250 nm. Therefore, no measurable bias is expected to occur from the particle-to-particle interactions[48].

### 3.6 Measurement uncertainty

The uncertainty analysis is conducted based on the single-point detection estimation proposed by Kline and McClintock [49]. The magnitudes of uncertainty for both 1-D and 3-D cases increase with increasing temperature, but the relative uncertainty magnitudes normalized by the corresponding measured MSD values are indeed decreasing. This is due to the fact that the MSD values increase more rapidly with increasing temperature.

The uncertainty of the Diffusion coefficient is expressed from Eq. (3) as:

$$\frac{w_D}{D} = \pm\left[\left(\frac{w_T}{T}\right)^2 + \left(\frac{w_\mu}{\mu}\right)^2 + \left(\frac{w_{r_p}}{r_p}\right)^2\right]^{1/2} \tag{10}$$

As a selected example at 25°C, $w_D/D$ is calculated to be ±4.06%, where the elementary contribution from the particle diameter uncertainty, the third term, is dominant over the contributions of the temperature and viscosity uncertainties.

## 4. Ratiometric Total Internal Reflection Fluorescent Microscopy (R-TIRFM)

### 4.1 Evanescent Wave Theory

At angles larger than the critical angle, $\theta_c=\sin^{-1}(n_t/n_i)$, $n_t>n_i$ at which the angle of refraction is 90°, light is completely reflected at the interface, i.e., the total internal reflection rather than passing through and refracting in accordance with Snell's law, and no significant amount is refracted into the bulk phase of the rarer medium. This description, however, is only true from the macroscopic point-of-view. However, from the microscale point-of-view, a portion of the incident light penetrates through the interface into the external medium, and propagates parallel to the surface in the plane of incidence creating an electromagnetic field in the liquid (the external medium) adjacent to the interface. This field, termed as the *evanescent field*, is capable of exciting fluorophores residing in the immediate region extremely near the interface. The evanescent wave intensity $I$ decays exponentially with the normal distance $z$ measured from the interface located at $z = 0$.

$$I(z) = I_0 \exp\left(-\frac{z}{z_p}\right), \qquad z_p = \frac{\lambda_0}{4\pi}\left(n_i^2\sin^2\theta - n_t^2\right)^{-\frac{1}{2}} \tag{11}$$

where $I_0$ is the incident light intensity at the interface and the penetration depth at $I/I_o = e^{-1}$ is determined by the incident wavelength in vacuum ($\lambda_o$) and the refractive indices of the internal and external mediums ($n_i$, $n_t$). With increasing $\theta$ the field intensity decays faster and the penetration depth $z_p$ is smaller. Note that for all incident angles, 10% intensity is reached within 300-nm range from the interface.

### 4.2 High NA Objective based TIRFM System

Traditionally, two different configurations of TIRFM are popular[14]. The first set up with a prism can be readily achieved and requires only the microscope, prism, and laser. The main drawback for this setup is the requirement that the specimen be positioned between the prism and the microscope objective and the higher order evanescent wave field must be used due to the geometrical

constraint, which substantially weakens the field intensity after repeated internal reflection modes. The second and presently preferred setup implements the laser to be illuminated through an inverted microscope, and greatly benefits from a special TIRF objective lens with a numerical aperture (NA) greater than 1.4.

Figure 7 shows the schematic illustration of the objective lens-based TIRFM system. An Olympus Plan APO 60X oil immersed TIRF lens with a NA of 1.45 is used for performing TIRFM experiments. The experimental setup consists of an inverted microscope (IX-50, Olympus Inc.), a 200-mW CW argon-ion laser (tuned at 488-nm, Laser Physics Inc.), a frame grabber board (QED Imaging Inc.), and particle tracking analysis software, which has been developed at the authors' Micro/Nano-Scale Fluidics and Heat Transport Laboratory [http://go.to/microlab]. The upper outlet port of the microscope is connected to the CCD camera. Tested nanoparticles are yellow-green (505 nm/515 nm) carboxylate coated fluorescent microsphere beads of 200-nm (±20-nm variance) diameter, which have a specific gravity of 1.05 and carry weekly negative charges because of their $COOH^-$ group attached to carboxylate (Molecular Probes Inc.). The specimen is placed on the upper surface of the 170-μm thick glass slip.

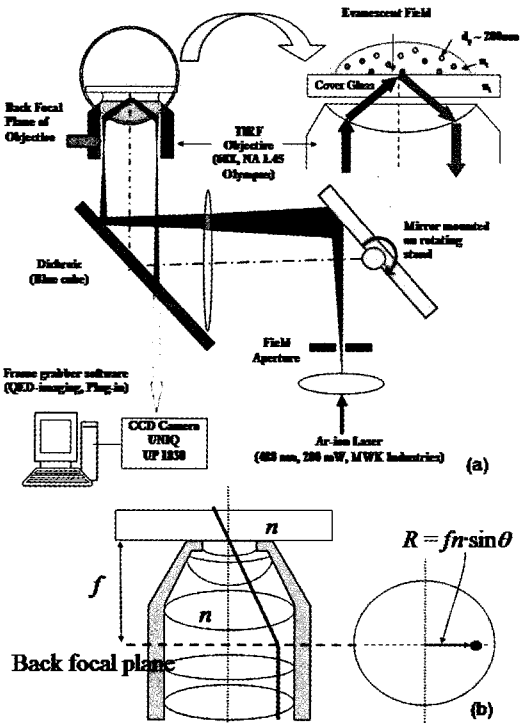


**Fig. 7.** (a) Schematic illustration of Total Internal Reflection Fluorescence Microscopy (TIRFM) setup with high-NA (oil-immersion type) objective lens, and (b) the illustration of calculation of the beam incident angle using a transfer function for the off-center laser beam location[46].

The critical angle for the lens with total internal reflection at a water-glass interface is $\theta_{critical} = \sin^{-1}(1.33/1.515) = 61.38°$. For an oil-based objective with 1.45 NA, the maximum angle of passage of light is $\sin^{-1}(NA/n_i) = \sin^{-1}(1.45/1.515) = 73.15°$[5]. The present optical configuration allows that the incident angles can be varied from $\theta_i = 62°$ ($z_p$ = 272 nm) to 68° ($z_p$ = 86 nm). Figure 8 provides a comparison between the direct and the evanescent wave illuminated images. Light scattering from out of focus particles causes significant background

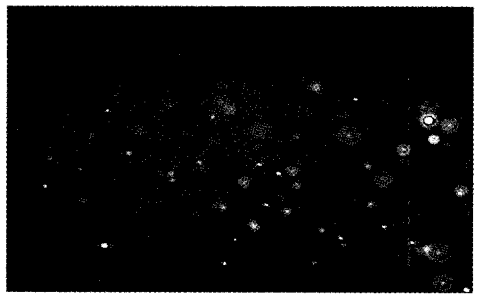

(a) Direct Illumination with $\theta_i = 60°$ ($\theta_{critical} = 61.38°$)

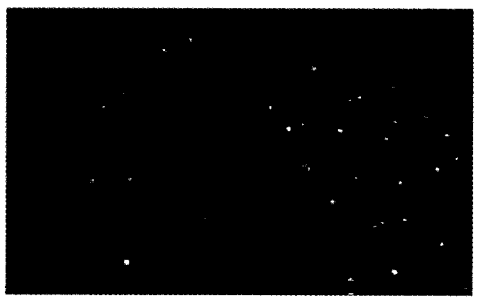

(b) Near Wall TIRFM Image with $\theta_i = 65°$ ($z_p$ = 114 nm)

**Fig. 8.** Comparison of direct illuminated image at an incident angle slightly below the critical angle (a), and evanescent wave illuminated image with an incident angle larger than the critical angle (b)[46].

noise for the case of refracted wave illumination for $\theta_i = 60° < \theta_{critical}$ (Fig. 8-a). The signal-to-noise ratio is substantially improved for the TIRFM image with $\theta_i = 65°$ because of the near-wall illumination thickness comparable to the penetration depth $z_p = 114$ nm (Fig. 8-b).

### 4.3 Ratiometric Imaging Analysis

The ratiometric imaging analysis for TIRFM images can provide critical information on the depth wise locations of nanoparticles in the near-wall region with nanometer resolution. Mathematical derivation of the ratiometric imaging analysis has been presented in details elsewhere[24]. The detected fluorescence signal at an arbitrary test field point ($x$, $y$) integrated in the line-of-sight direction $z$ through the microscope objective (Fig. 9), $F(x, y; z_p)$ can be described as

$$F(x,y;z_p) = \varepsilon \cdot I_0(x,y;z_p) \cdot \int_0^{\infty} [Q(z) \cdot P_D(z)] \cdot C(x,y,z) e^{\frac{z}{z_p}} dz \quad (12)$$

where $\varepsilon$ defines the quantum efficiency of fluorescent particles and of a CCD camera, which is assumed to be equal for all depth-wise locations $z$, and $I_0(x, y; z_p)$ is the illumination intensity at the coverslip glass-water interface. Performing detailed mathematical formulations by various authors[50,51], the normalized intensity detected by a CCD for a fluorescent particle of radius $R$ located at $h$ from the interface, as illustrated in Fig. 9, is expressed as

$$I_N(h,R,c) = \left(4\pi c z^3, \left[\left(\frac{R}{z_p}\right)\cosh\left(\frac{R}{z_p}\right) - \sinh\left(\frac{R}{z_p}\right)\right] \cdot e^{\frac{h}{z_p}}\right) \quad (13)$$

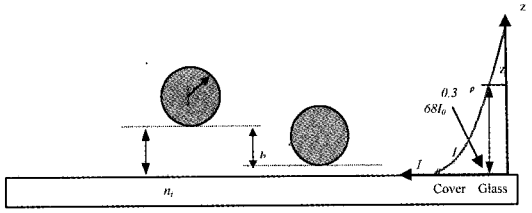


**Fig. 9.** Two nanoparticles at different z-locations schematically illustrating the Ratiometric Total Internal Reflection Fluorescence Microscopic (R-TIRFM) imaging analysis[46].

Although Eq. (13), in principle, can determine the particle location ($h$) by measuring $I_N$ under a specified penetration depth ($z_p$), in reality the fluorescence concentration function $c$ is difficult to measure and usually not accurately known. By taking the quotient of two recordings, the unknown fluorophore concentration $c$ can be eliminated. Thus, by taking the ratio of $I_N$ from two different particles at two different $z$-locations, the determination of their relative locations is more appropriate in that those unknown and fuzzy factors are cancelled out, i.e.,

$$RI \equiv \frac{I_N^1(h_1,R,c)}{I_N^2(h_2,R,c)} = \exp\left(-\frac{\Delta h}{z_p}\right) \quad (14)$$

To obtain the relative position $\Delta h$ of two particles from the Ratiometric Intensity $RI$ for the present experiment, care is taken to focus on a particle which is immobile at the glass-water interface and to consider the brightest particle location as the reference point of $z = 0$. The relative intensity of other particles in the image can now be identified to determine their depth-wise $z$-locations with respect to the reference zero point. The integrated and normalized intensity $I_N$, given in Eq. (13), is analogous to an average intensity of a detected particle image. However, it is difficult to integrate the individual pixels over the whole spot on the image. Thus, to determine the spot area intensity, a peak intensity is taken to be the representative value for the particle.

### 4.4 Results and Discussion

Results are presented for near-wall hindered Brownian diffusive motion measured in two-fold: (1) manual tracking of a single particle, and (2) digital image tracking of multiple particles based on particle paring using the neural network algorithm. An incident angle of 62° is used to create an evanescent field thickness $z_p$ of 272 nm for all the experiments. The incident angle is selected to ensure that the measurements are not restricted by the penetration depth itself. In other words, if the penetration depth is chosen to be smaller than the average Brownian displacement in the normal direction, the measured data can be severely biased

for underestimation since the limited illumination of the thin penetration depth will be unable to capture the entire movement of the particles.

Note that since only the maximum image intensity, corresponding to the closest pole of a particle from the solid surface, is detected and analyzed for R-TIRFM, the test particles are not limited to be smaller than the evanescent wave penetration depth. Cell biologists, surface chemists, and colloid scientists have successfully used evanescent wave microscopy to study motion of cells and colloids of size ranges from a few microns up to 10 μm[52,53]. Rohrbach[24] also used a 60-nm thick evanescent wave field to measure the location of a spatially fixed 300-nm particle using a similar technique. The current penetration depth of 272-nm should be sufficient to illuminate the 200-nm test particles.

In figure 10, an arbitrarily chosen single particle was tracked manually with the depth-wise resolution of 2.36 nm and the lateral resolution of 143.3 nm for consecutive 67 frames when it disappears beyond the effective visualization depth. As the distance of the particle from the interface increases, the intensity decreases exponentially until the particle vanishes totally. The particle is assumed to be beyond the effective visualization depth when the difference between its maximum pixel intensity and the surrounding pixel intensity approach within 10%. The apparently "random-walk" like Brownian movement seen in Fig. 10-a presents a solid evidence of near-wall hindrance as shown for *x-y-z* decomposed displacements in Fig. 10-b. Note that all individual displacements are random with nearly zero average displacement. While the *x*- and *y*- displacement shows virtually no distinction as they should be, the significantly reduced *z*-displacement evidences the hindered Brownian motion due to the presence of the solid wall.

Figure 11 shows the results of the entire population of particles for the total of 90 frames using the neural network based particle tracking algorithm. Figure 11-a presents the lateral displacements that are anisotropic and random on the *x-y* plane, and Figs. 11-b and c present the particle displacements on the normal *x-z* and *y-z* planes, respectively. The

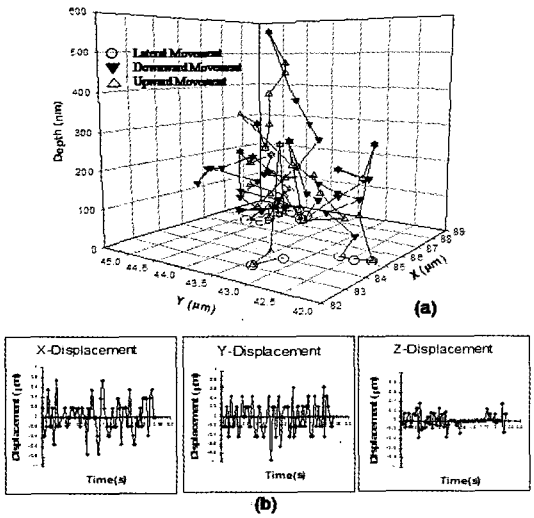


**Fig. 10.** Manual tracking of the Brownian motion of a single 200-nm particle suspended in water at 293K: (a) the history of three-dimensional locations over 67 imaging frames recorded for the duration of 2.23 s; and (b) the history of its *x-y-z* directional displacements[46].

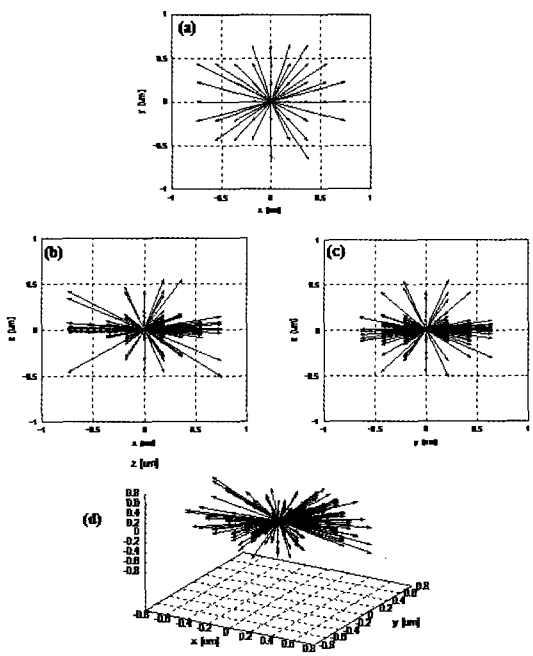


**Fig. 11.** Brownian diffusive displacements for multiple 200-nm particles tracked by the network model: the anisotropic displacements in the lateral *x-y* plane (a), the normally quenched displacements in the line-of-sight *x-z*, *y-z* planes (b and c), and the three-dimensional displacements (d)[46].

more pronounced reduction of particle displacements in the $z$-direction, in comparison with the lateral displacements in the $x$-$y$ plane, supports the theoretical predictions of hindered diffusion in the vicinity of a wall (Fig. 1). Figure 11-d presents vectors of three-dimensional displacements that are substantially quenched in the normal direction to conform to an oval shape because of the directional preference of the near-wall diffusive hindrance.

Both the single particle tracking data and the neural network based tracking data are then compared with the theoretical predictions and the results are summarized in Table 1. The parameters compared include the Mean Square Displacements (MSD), mean displacements, absolute mean displacements, and elementary ($D_\perp$, $D_{||}$) and bulk ($D_o$) diffusion coefficients, for 200 nm particles in water at $T$ = 293K and for the measurement time interval of 33 ms. While the theoretical isotropic diffusion coefficient is evaluated as $D$ = 2.1451 μm$^2$/s, all other presented theoretical values in Table 1 represent their near-wall hindered ones as shown in Eqs. (5), (6), and (7). The measured MSD values of $<\Delta x^2>$ and $<\Delta y^2>$, by both the single particle tracking and the neural network algorithm, compare well with the theoretical predictions. However, the measured values of $<\Delta r^2>$ are found to be slightly underestimating when compared with the theory, and this is primarily attributed to the discrepancy between the $<\Delta z^2>$ data and its theoretical predictions.

Since the measurement of the hindered MSD in the normal direction persistently underestimates the predictions, the discrepancy is believed to be the result of the physical inadequacy and limitation of the near-wall hindrance theory[28] for the present experimental conditions. The Brenner's analysis takes into consideration only the hydrodynamic interaction between a single sphere and the wall. The resulting correction coefficient for the normal diffusion $\xi$ does not take into account for additional hindering effects such as electrostatic and

**Table 1.** Comparison of theoretical predictions with measured data for Brownian motion of 200-nm particles in water at 20°C for a specified time interval of 33-ms [free diffusion coefficient ($D$), hindered elementary (normal: $D_\perp$, lateral: $D_{||}$), and hindered bulk diffusion coefficients ($D_o$)][46].

| Parameters | Units | Theory | Neural Network Based Multiple Particle Tracking Data | Single Particle Manual Tracking Data |
|---|---|---|---|---|
| | | Mean Square Displacement (MSD) | | |
| $< \Delta r^2 >$ | μm$^2$ | 0.2753 | 0.2517 | 0.2278 |
| $<\Delta x^2>$ | | 0.1022 | 0.1069 | 0.1024 |
| $<\Delta y^2>$ | | 0.1022 | 0.1234 | 0.1008 |
| $<\Delta z^2>$ | | 0.0709 | 0.0214 | 0.0246 |
| | | Brownian Diffusivity | | |
| D | μm$^2$/s | 2.1451 | - | - |
| $D_o$ | | 1.3765 | 1.2585 | 1.1390 |
| $D_{||}$ | | 1.5330 | 1.7273 | 1.5240 |
| $D_\perp$ | | 1.0635 | 0.3210 | 0.3690 |
| | | Mean Displacement | | |
| $< \Delta r >$ | μm | 0 | 0.0208 | 0.0244 |
| $<\Delta x>$ | | 0 | -0.0146 | 0.0167 |
| $<\Delta y>$ | | 0 | 0.0145 | -0.0176 |
| $<\Delta z>$ | | 0 | 0.0033 | 0.0030 |
| | | Mean of Absolute Displacement | | |
| $<\lvert\langle \Delta r \rangle\rvert>$ | μm | 0.5247 | 0.4548 | 0.3791 |
| $<\lvert\langle \Delta x \rangle\rvert>$ | | 0.3197 | 0.2987 | 0.2437 |
| $<\lvert\langle \Delta y \rangle\rvert>$ | | 0.3197 | 0.3339 | 0.2761 |
| $<\lvert\langle \Delta z \rangle\rvert>$ | | 0.2663 | 0.0786 | 0.0901 |

electro-osmotic forces between them. It is the authors' conjecture that the formation of an electronic double layer (EDL) on the cover glass surface plays a key part here. Based on the surface hydrolyzation, the EDL thickness or the so-called Debye length, ranges from 10 to 100-nm depending on the ionic concentration of the solution[54, 55].

The theoretical values of the elementary hindered diffusion coefficients ($D_\perp$, $D_{||}$) and bulk ($D_o$) diffusion coefficients are compared with the measured data. The theoretical diffusion coefficient $D_{||}$ is calculated based on either of the identical MSD in the $x$ and $y$ directions while the experimental $D_{||}$ is determined from the average of the measured $x$ and $y$ MSD values. Their comparison is seen to be in good agreement with each other. The measured normal diffusion coefficient $D_\perp$ is seen to be about one-third of the theoretically estimated value. From Brenner's theory, it is conjectured that the additional hindering be attributed to the electrostatic and electro-osmotic forces between the negatively charged nanoparticles and the negatively charged silanol surface of glass. It is uncertain, however, whether the pertinent effect is the sole reason for the excessive near-wall hindering or not. Certainly more elaborate future investigation will be necessary to examine this conjecture but it is considered as the outside of the present scope of work.

The mean particle displacement $<\Delta r>$, as well as $<\Delta x>$,$<\Delta y>$,$<\Delta z>$ should be zero because of the spherically symmetric random nature of the Brownian motion. The corresponding experimental data well manifests this random nature showing extremely small values. For the case of the mean absolute displacements $\left(\langle|\Delta r|\rangle \equiv \sum_N |\Delta r|_i / N\right)$, a fairly good agreement is shown for both the single particle results and the statistically enhanced results based on the particle tracking algorithm. Since no theoretical estimation is readily available, the square root of MSD is used to approximately predict the mean of absolute displacements. Nevertheless, these approximated theoretical values of $<|\Delta x|>$ and $<|\Delta y|>$ compares well with the corresponding experimental data.

However, a discrepancy is observed in the $<|\Delta z|>$ measurement because of the aforementioned physical reasons for additional hindering effects.

Finally, a comment should be made regarding the various measurement uncertainties associated with the R-TIRFM system. Measurement of $I_N$ by Eq. (13) involves a number of errors because of background noise in the image. The major errors are attributed to the background fluorescence and to the lateral scattering of the excitation light by the neighboring particles. These errors are largely eliminated by using a low concentration of the fluorophore in water (0.001% by volume at present) and keeping the penetration depth minimal to improve the image contrast. Another important uncertainty occurs in estimating $z_p$ because of the incident angle uncertainty, and the inaccurate refractive indices of the cover glass, the emersion oil, and the fluorophore solution. Additional errors can be caused by the uncertainty of the surface intensity because of the micro/nano-scale nonuniformities of the laser illumination. Indeed, some illumination nonuniformities are substantial as demonstrated in Fig. 8-b. However, most particles are fluctuating locally within the region of fairly uniform illumination intensity, so that their images minimally biased by the observed large-scale spatial nonuniformities. As for the temporal variations in the laser intensity, all experiments were performed after the laser beam was stabilized and fluctuations were within 0.1 mW. Furthermore, the intensity variation during such a relatively short imaging period of maximum four (4) seconds should be negligibly small.

It should be noted that for the overall uncertainty, the maximum error is associated with the mean error in the granule diameter for the fluorophores which is listed as 200 ± 20 nm (Molecular Probes, Inc.). A Kline McClintock[56] uncertainty analysis is performed by incorporating all these uncertainties to estimate the maximum uncertainty of ± 9.6% for the image intensity measurements and ± 19.3% for the particle locations.

## 5. Summary

An optical technique using diffraction images of Optical Serial Sectioning Microscopy (OSSM) was developed to determine the $z$-positions of monodispersed 500-mm nano-particles suspended in a thick

aqueous specimen. The experimental measurements were performed to validate the given theoretical model for the Point Spread Function (PSF) patterns. The micro chamber used in the Brownian motion measurement, consisted of a deep specimen and an off-designed cover glass. This created the aberration, and caused the asymmetric diffraction patterns. Using the theoretical PSF for an off-design condition, the nano-particles in the micro chamber were tracked with a lateral resolution of 0.16 μm and an axial resolution of 0.16 μm at 33-ms time intervals. The Brownian diffusivity of the nanoparticles and the Mean Square Displacement (MSDs) are measured for the temperature range from 5 to 70°C, and the results show fairly good agreement with the predictions with averaged discrepancies of 0.0036 $\mu m^2$ (5.55%), 0.0073 $\mu m^2$ (4.26%), and 0.0082 $\mu m^2$ (3.19%) for 1-D, 2-D, and 3-D cases, respec-tively. The line-of-sight Brownian motion detection using the OSSM technique, in lieu of the two-dimensional or the full three-dimensional Brownian motion tracking, shows good potential as a nonintrusive and microscale thermometry for nanoparticle suspension fluids.

A novel three-dimensional ratiometric particle tracking technique has been developed and applied to examine the hindered Brownian diffusion of 200-nm particles within the effective visualization thickness of 2 $z_p$ = 544 nm from the interface given at $\theta_i$ = 62°. Three-dimensional particle displacements are analyzed using a robust Neural Network Model identifying particle pairs across imaging frames. The technique is likely considered as the first of its kind to tag and track nano-particles in a full three-dimensional way with unprecedented nanometer spatial resolution. The spatial resolution of the particle displacement measurements is estimated as 143.33 nm in both *x*- and *y*- direction, and mere 2.36 nm in the *z*-direction. On the other hand, relatively smaller measurement uncertainties of 0.1 % are estimated in the lateral particle locations on the *x*-*y* plane, but rather large uncertainties of 19.3% for the particle locations in the *z*-direction. The measured Brownian diffusion behavior show fairly impressive agreement with the near-wall hindrance theory in the lateral *x*-*y* plane, but the measured diffusion coefficient in the *z*-direction shows approximately one-third of the theory, while the theory is based on the consideration of the pure hydrodynamic interaction of a single particle with the wall. In order to account for the present experimental findings, the authors propose to further examine the near-wall hindrance model by additionally incorporating non-hydrodynamic effects, such as electrostatic and electro-osmotic forces that may be prevalent within the penetration depth of the evanescent wave field.

## References


1) Xie S 2001 Single-molecule approach to enzymology. Single Mol 2: 229-236.
2) Weiss S 2000 Measuring conformational dynamics of bio-molecules by single molecule fluorescence spectroscopy. Nat Struct Bio7: 724-729.
3) Ishijima A and Yanagida T 2001 Single molecule nanobioscience. Trends in Biochem Sci 26: 438-444.
4) Lange FD, Cambi A, Huijbens R, Bakker BD, Rensen W, Parajo MG, Van Hulst N, and Figor CG 2001 Cell Biology beyond the diffraction limit: near field scanning optical microscopy. J Cell Sci 114: 4153- 4160.
5) Hecht E 2002 Optics, 4th edn. Addison Wesley, Massachusetts, 124-127.
6) Born M and Wolf E 1980 Principles of Optics, 6th edn. Cambridge University Press, Cambridge, 47-51
7) Agard DA 1984 Optical sectioning microscopy: cellular architecture in three dimensions *Ann. Rev. Biophys. Bioeng.* 13: 191-219.
8) Cagnet M, Francon M, and Thrierr JC 1962 *Atlas of optical phenomena* (Berlin: Springer -Verlag)
9) Richards B and Wolf E 1959 Electromagnetic diffraction in optical systems II. Structure of the image field in an aplanatic system *Proc. R. Soc.* A 253: 358-379.
10) Gibson F S and Lanni F 1991 Experimental test of an analytical model of aberration in an oil-immersion objective lens used in three-dimensional light microscopy *J. Opt. Soc. Am. A* 8: 1601-1613.
11) Inoué S and Spring KR 1997 *Video Microscopy: The Fundamentals* (New York: Plenum) 26-65.
12) McNally JG, Preza C, Conchello JA, and Thomas LJ 1994 Artifacts in computational optical-sectioning microscopy *J. Opt. Soc. Am. A* 11: 1056-1067.
13) Speidel M, Jonas A and Florin EL 2003 Three-dimensional tracking of fluorescent nanoparticles with subnanometer precision by use of off-focus imaging *Optics Letters* 28: 69-71
14) Axelrod D, Burghardt TP, and Thompson NL 1984 Total Internal reflection fluorescence (in biophysics). Annl Rev of Biophys and Bioengg 13: 247-268

15) Goos VF and Hanchen H 1947 Ein neuer und fundamentaler Versuch zur Totalreflexion. Ann Physik 1: 333-346.
16) Axelrod D, Hellen EH, and Fulbright RM 1992 Total Internal reflection fluorescence. In: Lakowicz J (ed) Topics in Fluorescence Spectroscopy: Principles and Applications. Vol.3: Biochemical Applications. Plenum Press, New York, 289-343.
17) Pawley JB 1995 Handbook of Biological Confocal Microscopy. 2nd Edn. Plenum Press, New York
18) Stelzer EHK and Lindek S 1994 Fundamental reduction of the observation volume in far-field light microscopy by detection orthogonal to the illumination axis: confocal theta microscopy. Opt Commun 111: 536-547.
19) Denk W, Strickler JH, and Webb WW 1990 Two photon laser scanning fluorescence microscopy. Science 248: 73-76.
20) Sako Y, Minoghchi S, and Uyemura T 2000 Single-molecule imaging of EGFR signaling on the surface of living cells. Nature Cell Bio 2: 168-172.
21) Sako Y and Yanagida T 2003 Single-molecule visualization in cell biology. Img Cell Bio: SS1-SS5.
22) Zettner CM and Yoda M 2003 Particle velocity field measurements in a near-wall flow using evanescent wave illumination. Exp Fluids 34: 115-121.
23) Jin S, Huang P, Park J, Yoo JY, and Breuer KS 2003 Near-Surface Velocimetry using Evanescent Wave Illumination. Proceedings of IMECE 2003:55015.
24) Rohrbach A 2000 Observing Secretory Granules with a Multiangle Evanescent Wave Microscope. Biophy J 78: 2641-2654.
25) Banerjee A, Chon C, and Kihm KD 2003 Nanoparticle tracking using TIRFM imaging. 2003 IMECE Photogallery
26) Einstein A 1905 On the motion, required by the molecular-kinetic theory of heat, of particles suspended in a fluid at rest *Ann. Phys.* (Leipzig) 17: 549-560.
27) Goldman AJ, Cox RG, and Brenner H 1967 Slow viscous motion of a sphere parallel to a plane-I: Motion through a quiescent fluid. Chem Engg. Sci 22: 637-651.
28) Brenner H 1961 The slow motion of a sphere through a viscous fluid towards a plane surface. Chem Engg Sci 16: 242-251.
29) Kim S and Karrila SJ 1991 Microhydrodynamics: Principles and Selected Applications. Butterworth-Heinemann: Portland
30) Olsen MG and Adrian R J 2000 Brownian motion and correlation in particle image velocimetry *Opt. & Laser Technol.* 32: 621-627.
31) Lawson AW and Long EA 1946 On the possible use of Brownian Motion for low temperature thermometry *Phys. Rev.* 70: 220-221.
32) Hohreiter V, Wereley ST, Olsen MG, and Chung JN 2002 Cross-correlation analysis for temperature measurement *Meas. Sci. Technol.* 13: 1072-1078.
33) Sato Y, Inaba S, Hishida K, and Maeda M 2003 Spatially averaged time-resolved particle-tracking velocimetry in microspace considering Brownian motion of submicron fluorescent particles *Exp. Fluids* 35: 167-177.
34) Ingenhousz J 1779 Experiments on vegetables, discovering their great power of purifying the common air in sunshine, and of injuring it in the shade or at night. Excerpts from Marshall H.L; Herbert S. K (1952) A Source Book in Chemistry: 1400-1900.
35) Brown R 1966 *The World of the Atoms*, edited by H. Boorse and L. Motz (New York: Basic Books) 1: 206-212.
36) Perrin JB, See [http://www/nobel.se/physics/laureates /1926/index.html] for Perrin's Nobel Prize acceptance speech.
37) Perrin JB 1990 *Atoms* (Ox Bow Press, New York) 109-133.
38) Nakroshis P, Amoroso M, Legere J, and Smith C 2002 Measuring Boltzmann's constant using video microscopy of Brownian motion *Am. J. Phys.* 71: 568-573.
39) Salmon R, Robbins C, and Forinash K 2002 Brownian motion using video capture *Eur. J. Phys.* 23: 1-5.
40) Deen WM 1998 Analysis of Transport Phenomenon. Oxford, New York, pp 59-63.
41) Fox RW, McDonald AT and Pritchard PJ 2004 *Introduction to Fluid Mechanics* (6th ed., Hoboken: John Wiley & Sons) 721-724.
42) Shlesinger MF, Klafter J, and Zumofen G 1999 Above, below and beyond Brownian motion. Am J Phys 67: 1253-1259.
43) Schatzel K, Neumann WG, Muller J, and Materzok B 1992 Optical Tracking of Brownian Particles. App Opt 31: 770-778.
44) Dufresne ER; Squires TM; Brenner MP; Grier DG (2000) Hydrodynamic coupling of two Brownian spheres to a planar surface. Phy Rev Lett 85: 3317-3320.
45) Batchelor GK 1975 Brownian diffusion of particles with hydrodynamic interaction. J Fl Mech 74: 1-29.
46) Kihm KD, Banerjee A, Choi CK, and Takagi T 2004 Near-wall hindered Brownian diffusion of nanoparticles examined by three-dimensional Ratiometric Total Internal Reflection Fluorescence Microscopy (3D R-TIRFM) Experiments in Fluids 37:811-824
47) Mills AF 1999 *Heat transfer* (2nd ed., Prentice Hall) 333-340.
48) Russel WB, Saville DA, and Schowalter WR 1989 Colloidal dispersions (1st ed., Cambridge University Press) 21-63.
49) Kline SJ and McClintock FA 1953 Describing uncertainties in single-sample experiments *Mechanical Engineering* 75: 3-8.
50) Burghart TP and Thompson NL 1984 Effects of planar dielectric interfaces on fluorescence emission

and detection. Biophys J 46: 729-737.
51) Hellen EH and Axelrod D 1986 Fluorescence emission at dielectric and metal film interfaces. J Opt Soc Am B 4: 337-350.
52) Prieve DC 1999 Measurement of colloid forces with TIRM. Advances in Colloid and Interface Science 82: 93-125.
53) Bevan MA and Prieve DC 2000 Hindered diffusion of colloidl particles very near to a wall: revisited. Journal of Chemical Physics 113(3): 1228-1236.
54) Probstein RF 1994 Physicochemical Hydrodynamics. John Wiley & Sons Inc, New York
55) Kim MJ, Beskok A, and Kihm KD 2002 Electro-osmosis-driven micro-channel flows: a comparative study of microscopic particle image velocimetry measurements and numerical simulations. Exp Fluids 33: 170-180.
56) Kline SJ and McClintock FA 1953 Describing uncertainties in single-sample experiments. Mechanical Engineering 75(1): 3-9.
57) Park JS, Choi CK, and Kihm KD 2005 Temperature Measurement for Nanoparticle (500-nm) Suspension by Detecting the Brownian Motion Using Optical Serial Sectioning Microscopy (OSSM). Meas. Sci. Technol. 16: 1-12.